Microporosity Prediction in Aluminum Alloy Castings

A.S. SABAU and S. VISWANATHAN

A comprehensive methodology that takes into account solidification, shrinkage-driven interdendritic fluid flow, hydrogen precipitation, and porosity evolution has been developed for the prediction of the microporosity fraction and distribution in aluminum alloy castings. The approach may be used to determine the extent of gas and shrinkage porosity, *i.e.*, the resultant microporosity which occurs due to gas precipitation and that which occurs when solidification shrinkage cannot be compensated for by the interdendritic fluid flow. A solution algorithm in which the local pressure and microporosity are coupled is presented, and details of the implementation methodology are provided. The models are implemented in a computational framework consistent with that of commonly used algorithms for fluid dynamics, allowing a straightforward incorporation into existing commercial software. The results show that the effect of microporosity on the interdendritic fluid flow cannot be neglected. The predictions of porosity profiles are validated by comparison with independent experimental measurements by other researchers on aluminum A356 alloy test castings designed to capture a variety of solidification conditions. The numerical results reproduce the characteristic microporosity profiles observed in the experimental results and also agree quantitatively with the experimentally measured porosity levels. The approach provides an enhanced capability for the design of structural castings.

I. INTRODUCTION

THE use of aluminum alloy castings for structural components offers significant opportunities for reducing the weight of automobiles, since aluminum alloy components are typically about half the weight of the steel, cast iron, or ductile iron component that they replace. However, the performance requirements of structural castings, particularly chassis or suspension components, place greater requirements on their mechanical properties. An important factor that leads to a decrease in the mechanical properties of castings (notably ductility and fatigue life) is the presence of microporosity.

In the terminology commonly used by foundrymen, porosity is usually considered to be either "hydrogen" or "shrinkage" porosity. Hydrogen porosity is the term given to porosity that is generally rounded, isolated, and well distributed. Porosity that is interconnected or clustered and of an irregular shape corresponding to the shape of the interdendritic region is usually termed shrinkage. In general, the occurrence of microporosity in aluminum alloys is due to the combined effects of solidification shrinkage and gas precipitation.[1] Gas pores form when the partial pressure of hydrogen, which corresponds to the hydrogen concentration within the liquid, exceeds the local pressure in the mushy zone by an amount necessary to overcome surface-energy forces.[1] The local pressure in the mushy zone (P_m) results from (1) the ambient pressure, (2) the metallostatic head, and (3) resistance to the flow of fluid to feed solidification shrinkage.

Attempts to predict the level of porosity in castings have included both parametric[2–7] and continuum models.[1,8–12] A number of other studies have also attempted to understand the phenomena of porosity formation and pore growth[13,14,15] and pore morphology.[16]

Kubo and Pehlke[9] presented a methodology for the prediction of microporosity distribution in shaped castings. In their study, the effects on porosity formation of both the hydrogen precipitation during solidification and the pressure drop due to the feeding resistance of the mushy zone were considered. The pressure drop during solidification was calculated only in the interdendritic-feeding regime using Darcy's law. The liquid-feeding and mass-feeding regimes were neglected. The local pressure and porosity were computed in an uncoupled manner. The primary variable to be computed (either pressure or porosity) was selected based on a "flux of interdendritic liquid" criterion. If the flux of liquid was positive, then the pressure was first computed using the porosity at the previous time step. If the flux of liquid was negative, then the porosity was first computed using the pressure at the previous time step. The methodology proposed by Kubo and Pehlke[9] has been used with little change in numerous studies, such as those of Combeau *et al.*[17] and Rousset *et al.*[18]

The accuracy of the pressure computation is very important for microporosity prediction. The pressure distribution in castings is affected by liquid feeding, mass feeding, and by macroshrinkage effects such as the profile of the air-liquid metal interface in the riser, which cannot be considered using Darcy's law as the momentum equation. More accurate fluid-flow models than that used by Kubo and Pehlke[9] are presented by Zou and Doherty[19] and Combeau *et al.*[20] The former study considers porosity for two-dimensional cases. Without considering microporosity, the latter study includes interdendritic flow for three-dimensional simulations of mold filling. Suri and Paul[12] presented a three-dimensional methodology without providing details on the coupling between the computations of microporosity and pressure. Barkhudarov, *et al.*[11] suggested that the complexity of the Kubo and Pehlke method could be a limiting factor in its applicability to the simulation of fully three-dimensional castings.

A.S. SABAU, Research Staff Member, and S. VISWANATHAN, Project Leader, are with the Metals and Ceramics Division, Oak Ridge National Laboratory, Oak Ridge, TN 37831-6083.

Manuscript submitted January 4, 2001.

The governing equations for fluid flow and hydrogen evolution indicate that porosity formation and fluid flow are strongly coupled. However, in most studies on microporosity,[10,14,15] it is considered that the porosity formation does not influence the fluid flow in the mushy zone. Kuznetsov and Vafai[21] showed that neglecting the effect of porosity formation on the pressure in the mushy zone yields higher pressure drops and an over-prediction of final porosity. They also showed that the influence of porosity formation on the pressure is larger at lower pressures in the mushy zone.

Microporosity defects generally occur together with other defects such as macrosegregation and macroshrinkage. The appearance of these defects may be strongly coupled, *i.e.*, they may have a strong effect on microporosity, which, in turn, can influence their location and extent. By using an empirical model for microporosity growth, Sundarraj and Voller[22] found that inverse segregation depends strongly on microporosity. They found that microporosity influences inverse segregation by reducing the shrinkage feeding and, thereby, reducing the mass-flow rate of solute toward the solidifying regions. Therefore, in order to predict casting defects accurately, comprehensive models of fluid dynamics, heat transfer, solidification, and microporosity must be used.

To date, no methodology has been proposed to quantify the extent of shrinkage porosity, which occurs when solidification shrinkage cannot be compensated for by interdendritic fluid flow. In this study, we propose a methodology to determine the extent of gas and shrinkage porosity, based on experimental evidence and thermodynamic considerations. The methodology for microporosity prediction can be integrated into general computational frameworks for predicting casting defects. In order to accurately model the flow field for any casting condition, the fluid-dynamics model includes the liquid-feeding and mass-feeding regimes. The methodology presented in this study considers the following factors that contribute to microporosity formation: (1) heat transfer and alloy solidification, (2) the local microstructural-length scale, (3) hydrogen redistribution during solidification, (4) fluid flow, which feeds the solidification shrinkage, (5) bubble nucleation after surface-tension forces are overcome, (6) microporosity growth due to the local pressure drop in the mushy zone, and (7) pore expansion in regions where liquid feeding alone cannot compensate for the solidification shrinkage.

The solution algorithm presented includes a fully coupled, implicit treatment of microporosity and local pressure in the mushy zone. The methodology presented is suitable for straightforward implementation in commonly used algorithms for fluid dynamics (SOLA[11] and SIMPLE) in casting simulation software. The approach presented has been validated on aluminum A356 alloy test castings designed to capture a variety of solidification conditions.

II. HEAT TRANSFER AND ALLOY SOLIDIFICATION

The energy equation that describes the heat transfer during alloy solidification appears as

$$\frac{\partial \overline{\rho h}}{\partial t} + \nabla \cdot (\rho_l h_l g_l \mathbf{u}) = \nabla (k_{\text{eff}} \nabla T) \qquad [1]$$

where ρ, h, t, g, and T are the density, enthalpy, time, volumetric fraction, and temperature, respectively. The term $\overline{\rho h} = g_l \rho_l h_l + g_s \rho_s h_s + g_{se}(\rho_{se} h_{se} - \rho_s h_s)$ is the density-weighted enthalpy, $\mathbf{u}$ is the *intrinsic* fluid velocity, and $k_{\text{eff}} = k_s g_s + k_l g_l$ is the effective thermal conductivity. The subscripts s and l refer to the solid and liquid phases, respectively, while the subscript e indicates eutectic phases. The subscript se refers to the solid eutectic phase. Because we are mainly concerned with the numerical simulation of shrinkage-induced flows for which interdendritic velocities are small, the convection term is neglected in the energy equation. By neglecting the microsegregation in the solid, the enthalpies are given by

$$h_s(T) = \int_{T_0}^{T} C_p^s dT \qquad \text{and}$$
$$h_l(T) = h_s(T_E) + \int_{T_E}^{T} (C_p^l - C_p^s) dT + L \qquad [2]$$

where T_0 and T_E are the reference and eutectic temperature, respectively; C_p^s and C_p^l are the specific heat for the solid and liquid phase, respectively; and L is the latent heat of solidification.

III. FLUID DYNAMICS DURING CASTING

During solidification in alloy castings, regions of solid, mush, and bulk fluid coexist. At low solid fractions, solid nuclei are dispersed in the liquid and carried away by the liquid metal flow. This flow regime, in which the alloy behaves like a slurry, is referred to as mass feeding. At solid fractions larger than a critical value (g_s^{cr}), referred to as the coherency limit, dendrites form a fixed network through which the liquid metal flows. The value of g_s^{cr} is dependent on the type of alloy and dendrite morphology.[23] The flow regime encountered above the coherency limit is called interdendritic feeding.

In order to determine the pressure drop during solidification, various feeding mechanisms such as liquid feeding, mass feeding, and interdendritic feeding must be considered.[24] In order to consider mass and interdendritic feeding, the alloy volumetric fraction (g_c) and alloy density (ρ_c), which are convected by the liquid flow, are tracked. The g_c and ρ_c variables are given by

$$g_c = \begin{cases} 1 \text{ if } g_s \le g_s^{cr} \\ g_l \text{ if } g_s > g_s^{cr} \end{cases} \text{ and } \rho_c = \begin{cases} \overline{\rho} \text{ if } g_s \le g_s^{cr} \\ \rho_l \text{ if } g_s > g_s^{cr} \end{cases} \qquad [3]$$

The mass-conservation equation for the intrinsic fluid velocity ($\mathbf{u}$) is given by

$$\frac{\partial \overline{\rho}}{\partial t} + \nabla \cdot (\rho_c g_c \mathbf{u}) = 0 \qquad [4]$$

where $\overline{\rho} = \rho_l g_l + \rho_s g_s + g_{se}(\rho_{se} - \rho_s) + \rho_g g_g$ is the volumetric average density; g_s, g_l, and g_g are the volume fraction of solid, liquid, and gas, respectively; and ρ_{se} and g_{se} are the density and volume fraction of the solid eutectic, respectively. The solid density (ρ_s) is usually taken to be constant, while the liquid density varies with the solute concentration and temperature, *i.e.*, $\rho_l = \rho_l(T, C_l)$. The gas density (ρ_g) varies according to the ideal gas law: $\rho_g = P_g/(R_{H_2} T)$, where R_{H_2} is the hydrogen gas constant.

Constant liquid and solid densities are considered in most

studies that deal with shrinkage effects during solidification. It is only recently that accurate modeling of the shrinkage demand during solidification was considered by employing variable liquid and solid densities as a function of temperature and concentration.[25,26]

The momentum equation for the interdendritic flow can be written as

$$\rho_c \left(\frac{\partial \mathbf{u}}{\partial t} + (\mathbf{u} \cdot \nabla)\mathbf{u} \right) = -\nabla P + \mu \nabla^2 \mathbf{u} + \rho_c g - g_l C_D \mathbf{u} + \mathbf{u} \frac{\partial}{\partial t} ((1 - g_c)\rho_s) \quad [5]$$

In general, the drag coefficient (C_D), which accounts for the momentum loss due to the flow around and through the dendrite structures, is a function of the viscosity (μ), the magnitude of velocity ($|\mathbf{u}|$), permeability (K_s), and liquid fraction (g_l). In this work, the drag coefficient is given by the Darcy's and Forchheimer's terms, which are often referred to as the "viscous-drag" and "form-drag" terms.[27]

$$C_D(|\mathbf{u}|, K_s, g_l) = \underbrace{\frac{\mu}{K_s}}_{\text{Darcy's}} + \underbrace{\frac{C_F \rho_c g_l}{\sqrt{K_s}} |\mathbf{u}|}_{\text{Forchheimer's}} \quad [6]$$

The Forchheimer's term must be considered when relatively high interdendritic fluid-flow velocities are expected. Such high velocities may be important during the intensification phase in die or squeeze casting.

IV. PERMEABILITY IN THE MUSHY ZONE

The Kozeny–Carmen equation[28–31] is used to relate the alloy permeability (K_S) to microstructural parameters:

$$K_s = \frac{g_l^3}{k_C S_V^2} \quad [7]$$

where g_l is the volumetric fraction of the liquid, k_C is the Kozeny–Carman constant, and S_V is the surface area of the solid per unit volume. The value of k_C is taken to be equal to 5.[31] Based on stereological considerations, S_V is defined as a function of dendrite cell spacing as $S_v = 4/d_c$.

In order to use the Kozeny–Carman equation at large liquid fractions, Han and Viswanthan[32] suggested that the dendrite coherency point must be taken into account when computing S_v. Another difficulty with the application of the Kozeny–Carman equation lies in the fact that the permeability decreases to zero as the liquid fraction decreases to zero. In order to limit the permeability to nonzero values, it is a common practice to consider that the permeability is limited by a certain threshold liquid fraction (g_l^{th}), whose value is, in general, chosen arbitrarily. For those alloys that exhibit isothermal eutectic reactions, the solidification front is planar and the area open to fluid flow is constant. Consequently, the liquid fraction that is used for permeability computations should be taken to be constant during the eutectic reaction.[32] For aluminum A356 alloys, an isothermal ternary eutectic reaction occurs at a 0.05 liquid fraction. Therefore, the liquid-fraction threshold for the permeability computation in this work is set at 0.05. In general, g_l^{th} can be taken to be equal to the eutectic fraction (g_e) for eutectic alloys.

Another implication of considering microstructural evolution during the eutectic reaction for the computation of interdendritic flows involves the application of (no)-slip boundary conditions.[33] In order to solve the momentum and mass-conservation equations within the bulk-liquid or mushy regions, boundary conditions must be prescribed for the pressure and velocity at interfaces between the mushy and solid regions. Without explicitly tracking the solidified interfaces within computational cells, boundary conditions can simply be applied at cell faces shared between solidified cells and mushy-zone cells. The no-slip boundary conditions, which are applied at the face center of an interfacial cell (f), appear as

$$\mathbf{u} = 0 \text{ and } \mathbf{n}_f \cdot \nabla P = 0 \quad [8]$$

where $\mathbf{n}_f$ denotes the cell-face normal. A cell is considered fully solidified when the liquid fraction in that cell becomes less than a critical liquid fraction (g_l^f). Values for the feeding threshold (g_l^f) vary between 0.1 and 0.01, and its choice is rather arbitrary.[34,35] However, the choice of g_l^f can be made on considerations of the eutectic microstructure. In many aluminum alloys, the final eutectic occurs at an invariant temperature, and the eutectic front moves as a sharp interface in the direction given by the eutectic isotherm. If the diffusion into the dendrites during the eutectic reaction is neglected, the dendrites coarsen at a constant volume fraction as the eutectic front moves through them. In the final eutectic regions, the volumetric liquid fraction is initially g_e, and the region of bulk solid extends for more than half the cell when $g_l \leq g_e/2$. In these cases, the cell center becomes located in the bulk solid region. Since the pressure is not computed in regions of bulk solid in this study, including those cells in which $g_l \leq g_e/2$, the value for the feeding threshold is estimated to be $g_l^f = g_e/2$.[33]

V. MICROSTRUCTURAL PARAMETERS

In addition to the liquid and solid fractions, which are calculated from the energy equation, the dendrite cell spacing is needed to estimate pore curvature and permeability in the mushy zone. For the A356 aluminum alloy, the dendrite cell spacing (d_c) is correlated with the local solidification time (t_f) by the use of the relationship[36]

$$d_c = 10.2\, t_f^{0.33} \quad [9]$$

where d_c is in microns, and t_f is the local solidification time in seconds.

In most studies on microporosity, the pore radius (r) is taken to be proportional to the dendrite cell spacing through the following relationship:

$$r = g_\sigma d_c/2 \quad [10]$$

where g_σ is a pore-curvature factor.

In the absence of a rigorous constitutive model for the pore radius, empirical correlations have been used in other studies. Shivkumar *et al.*[14] assumed that the pore diameter was half the secondary dendrite arm spacing. Based on geometrical considerations for the arrangement of dendrites in an equiaxed microstructure for an Al-4.5Cu alloy, Poirier *et al.*[10] assumed that the pore-curvature factor was variable and dependent at any instant on the liquid fraction. Results of Fang and Granger[13] indicate that the pore-curvature factor is

variable. For a hydrogen content of 0.3 cc /100 g, an initial value of 0.15 for the pore-curvature factor was found to be appropriate. Based on microstructural observations that the pore diameter is approximately equal to the dendrite cell spacing, the pore-curvature factor for an aluminum A356 alloy is taken to be equal to the one in this study.

VI. HYDROGEN-POROSITY EVOLUTION

It is commonly accepted that pores form in solidifying aluminum alloys when the equilibrium partial pressure of hydrogen, corresponding to the hydrogen concentration within the liquid, exceeds the local pressure in the mushy zone by an amount necessary to overcome surface-energy forces.[1] Thus, the condition for microporosity formation is given in terms of a pressure condition, as

$$P_g \geq P_m + P_\sigma \qquad [11]$$

where P_g is the gas pressure corresponding to the gas concentration in the liquid, P_m is the local pressure in the solidifying alloy, and $P_\sigma = 2\sigma/r$ is the pressure due to surface tension. The local pressure in the mushy zone (P_m) results from (1) the ambient pressure, (2) the metallostatic head, and (3) resistance to the flow of fluid to feed solidification shrinkage. The term σ is the surface tension at the gas-liquid interface, and r is the pore curvature.

Since the molten metal used in most foundries has a high concentration of oxide films that serve as nucleating substrates for hydrogen bubble nucleation, detailed models of bubble nucleation may be neglected. Once bubbles form, the condition for the hydrodynamic balance of pressure in the bubbles is $P_g = P_m + P_\sigma$. Neglecting its diffusion, hydrogen evolution is described by the following mass balance:

$$f_g C_{\mathrm{H}}^u = C_{\mathrm{H}}^0 - C_{\mathrm{H}}^l (f_s k_{\mathrm{H}} + f_l) \qquad [12]$$

where C_{H}^0 is the initial gas concentration within the liquid (in cc/100 g), $k_{\mathrm{H}} = 0.069$ is the partition coefficient for hydrogen between solid and liquid,[10] and f_s and f_l are the mass fractions of solid and liquid, respectively. The hydrogen concentration in the liquid (C_{H}^l) and the gas pressure P_g (in atmospheres) are related through Sievert's law as $C_{\mathrm{H}}^l = S\sqrt{P_g}$, where S is the hydrogen solubility in the liquid (in cc/100 g) in equilibrium with hydrogen at atmospheric pressure. Using $C_{\mathrm{H}}^u = 8.92 \times 10^{-7}$, a constant for converting measurements from cc/100 g to mass fractions, the hydrogen evolution is described by the following mass-balance equation:

$$f_g C_{\mathrm{H}}^u = C_{\mathrm{H}}^0 - S\sqrt{P_m + P_\sigma}\,(f_s k_{\mathrm{H}} + f_l) \qquad [13]$$

VII. DENSITY VARIATION AND SHRINKAGE

In this section, relationships are presented for the computation of density variation, or shrinkage, during a computational time step. The relationships presented are of general applicability and can be used for cases that include the effects of microsegregation and macrosegregation.

In this article, volumetric phase fractions (rather than mass fractions) were chosen as the primary variables to estimate the density, shrinkage, and liquid permeability for the computation of pressure in the mushy zone. Due to the complexity of the system of governing equations, it is difficult to solve the energy-, momentum-, and mass-conservation and hydrogen-evolution equations in an implicit fashion. Accordingly, the energy and microporosity equations are uncoupled. The energy equation is solved using the hydrogen gas fraction at the previous time level (g_g^n), *i.e.*, without considering the effect of pore growth within the current time step. Because the volumetric fractions of the solid and liquid phases obtained after solving the energy equation do not consider the effect of pore growth, their values cannot be used to directly compute the liquid permeability, shrinkage, and pressure in the mushy zone. Therefore, in order to determine the current alloy density and its shrinkage and to accurately describe the hydrogen evolution, analytical expressions that deal implicitly with the pore growth at the current time level must be considered.

The mass balance for the volumetric fractions that are obtained from the energy (and solute) equations is given as $g_l^{*n+1} + g_s^{*n+1} + g_g^n = 1$, while the mass balance at the current time level is given as $g_l^{n+1} + g_s^{n+1} + g_g^{n+1} = 1$. The superscript $n + 1$ indicates the new time level, while the superscript asterisk indicates that the volumetric phase fractions, which are computed from the energy equation, are not the final values for the current time step. Due to the large difference in density between the gas and either the solid or liquid phases, mass fractions of the solid and liquid phases do not depend on the pore fraction when the pore fractions are not very large (*i.e.*, $g_g \leq 0.9$), and the following density relationships are valid:

$$\begin{aligned} &\overline{\rho} = \overline{\rho}_0(1 - g_g) \\ &g_l = f_l \frac{\overline{\rho}}{\rho_l}, \quad g_s = f_s \frac{\overline{\rho}}{\rho_s}, \quad \text{and} \quad g_{se} = f_{se} \frac{\overline{\rho}}{\rho_{se}} \end{aligned} \qquad [14]$$

where $\overline{\rho}$ is the average density of all phases in a computational element, $\overline{\rho}_0$ is the density of the alloy in the absence of porosity, and f and g denote mass and volumetric phase fractions, respectively. Using Eq. [14], the following relationships can be derived between the volumetric fractions that are computed from the energy equation and those at the current time step:

$$g_l^{n+1} = (1 - g_g^{n+1}) \frac{g_l^{*n+1}}{1 - g_g^n}, \quad g_s^{n+1} = (1 - g_g^{n+1}) \frac{g_s^{*n+1}}{1 - g_s^n},$$

$$\text{and} \quad g_{se}^{n+1} = (1 - g_g^{n+1}) \frac{g_{se}^{*n+1}}{1 - g_g^n} \qquad [15]$$

By denoting $\overline{\rho}^{*n+1}$ as the density that is estimated based on volumetric fractions computed from the energy equation, the average density at the current time step can be computed as

$$\begin{aligned} \overline{\rho}^{n+1} &= \overline{\rho}^{*n+1} + \overline{\rho}^{*n+1} \frac{g_g^n - g_g^{n+1}}{1 - g_g^n} \\ \overline{\rho}^{*n+1} &= \rho_l^n g_l^{*n+1} + \rho_s g_s^{*n+1} + g_{se}^{*n+1} (\rho_{se} - \rho_s) \end{aligned} \qquad [16]$$

The first term in the previous equation describes the contraction/expansion due to the solidification alone (*i.e.*, in the absence of pore growth during the current time step), while the second term describes the pore expansion during the current time step.

VIII. MICROPOROSITY GROWTH AND INTERDENDRITIC PRESSURE

In this section, the mathematical model for interdendritic flow and microporosity growth is derived. During solidification, the local pressure restricts pore growth, while pore growth leads to a lower shrinkage demand, which yields lower pressure drops in the mushy zone. Thus, pore growth and liquid feeding balance each other, as evidenced from the governing Eqs. [4], [5], [13], and [14] for the mass and momentum conservation, hydrogen evolution, and average density. In order to accurately predict microporosity, the solution algorithm used must be capable of handling the implicit coupling between pore growth and liquid feeding.

In this study, the solution algorithm for interdendritic flows is based on a variable projection method, *e.g.*, SOLA.[11] The variable projection method was developed to exactly enforce the constraint given by mass conservation (Eq. [4]) by applying the projection to the volumetric-averaged momentum of the convected alloy. The drag terms are treated implicitly in order to remove the severe time-step restrictions associated with semi-implicit discretizations.

An intermediate velocity (**u***) is computed from the momentum equation as

$$\rho_C \left(\frac{\mathbf{u}^* - \mathbf{u}^n}{\Delta t} + \mathbf{u} \cdot \nabla \mathbf{u} \right) = \mu \nabla^2 \mathbf{u}^n + \rho_C \mathbf{g} - \rho_s \frac{\partial g_C}{\partial t} \mathbf{u}^n - g_l C_D(|\mathbf{u}^n|, K_S, g_l)\mathbf{u}^* \quad [17]$$

Using the density relationship, the projection step is comprised of the following update of the pressure and velocity:

$$\nabla(\sigma_p \nabla P^{n+1}) = \frac{1}{\Delta t} \left(\frac{\overline{\rho}^{*n+1} - \overline{\rho}^n}{\Delta t} + \nabla \cdot (\rho_c^n g_c^n \mathbf{u}^*) + \frac{\overline{\rho}^{*n+1}}{\Delta t} \frac{g_g^n - g_g^{n+1}}{1 - g_g^n} \right) \quad [18]$$

and

$$g_c^n \rho_c^n \frac{\mathbf{u}^{n+1} - \mathbf{u}^*}{\Delta t} = -\sigma_p \nabla P^{n+1} \quad [19]$$

where the projection variable is given by

$$\sigma_p = \frac{g_C}{1 + g_l C_D \Delta t / \rho_C} \quad [20]$$

The terms in the right-hand side of the pressure equation (Eq. [18]) represent (1) the solidification-shrinkage effects in the current time step, neglecting microporosity growth, (2) the effect of inertia, viscosity, and gravity, and (3) pore-expansion effects within the current time step, respectively. For the sake of simplicity, we denote the first two terms in the right-hand side of the pressure equation by RHS_0, *i.e.*,

$$RHS_0 = \frac{1}{\Delta t} \left(\frac{\overline{\rho}^{*n+1} - \overline{\rho}^n}{\Delta t} + \nabla \cdot (\rho_c^n g_c^n \mathbf{u}^*) \right) \quad [21]$$

In the previous pressure relationships, the drag term and projection variable are computed using the liquid fraction available, *i.e.*, g_l^{*n+1}, which does not consider pore growth within the current time step. At high liquid fractions, where either microporosity has not yet nucleated ($g_l^{*n+1} = g_l^{n+1}$) or the porosity growth is small, the projection variable can be computed based on the liquid fraction computed from the energy equation (g_l^{*n+1}). At low liquid fractions, after porosity has nucleated, we must compute the projection variable based on g_l^{n+1} and not on g_l^{*n+1}. At low liquid fractions, when pore growth becomes important and the drag term is given by the Darcy term, the pore growth in permeability computations can be implicitly taken into account by using the following relationship for the pressure:

$$\nabla(\sigma_p^{*n1} \nabla P^{n+1}) = RHS_0 + G(P) \quad [22]$$

where the pore-growth term ($G(P)$) is given by the following relationship as a function of the pore expansion within the current time step:

$$G(P) = \left(\frac{\overline{\rho}^{*n+1}}{\Delta t^2} - 3RHS_0 \right) \frac{g_g^n - g_g^{n+1}}{1 - g_g^n} \quad [23]$$

Equations [13] and [14], for the density and hydrogen evolution, respectively, can be used to relate the pore growth with the pressure in the following way. First, using the density relationships, the hydrogen-evolution relationship can be written in terms of volumetric fractions as

$$g_g \rho_g C_{\mathrm{H}}^u = \overline{\rho} C_{\mathrm{H}}^0 - S\sqrt{P_m + P_\sigma}\,((g_s \rho_s + g_{se}(\rho_{se} - \rho_s))k_{\mathrm{H}} + g_l \rho_l) \quad [24]$$

Second, using Eqs. [15], [16], and [24] for the volumetric fractions and average density, the following expression can be derived for the pore-growth term:

$$\frac{g_g^n - g_g^{n+1}}{1 - g_g^n} = \frac{-\overline{\rho}^{*n+1} C_{\mathrm{H}}^0 + S\sqrt{P + P_\sigma}(\overline{\rho}^{*n+1} k_{\mathrm{H}} + g_l^{*n+1} \rho_l^{n+1}(1 - k_{\mathrm{H}})) + C_{\mathrm{H}}^u \rho_g^{n+1} g_g^n}{C_{\mathrm{H}}^0 \overline{\rho}^{*n+1} - S\sqrt{P + P_\sigma}(\overline{\rho}^{*n+1} k_{\mathrm{H}} + (1 - k_{\mathrm{H}}) g_l^{*n+1} \rho_l^{n+1}) + C_{\mathrm{H}}^u \rho_g^{n+1}(1 - g_g^n)} \quad [25]$$

This relationship is used to account for microporosity growth in the pressure equation. The pore-growth term is highly nonlinear as a function of pressure. In order to discretize the pressure equation (Eq. [23]), the pore-growth term must be linearized. The computational cycle for pressure computations is shown in Figure 1.

IX. PLATE CASTINGS

In order to capture the wide range of solidification conditions encountered in foundry castings, plate castings were made in a variety of mold configurations. Of those, three castings were of particular interest to this study. They included a plate cast in a sand mold without chills, a plate cast with an end chill, and one cast with top, bottom, and end chills. In the following sections, they will be referred to as the sand plate, end-chilled plate, and chill plate, respectively. The chill-plate configuration and casting dimensions are shown in Figure 2. The top and bottom chill dimensions were nominally 20 × 15 × 2.5 cm. The end-chill dimensions were nominally 6 × 15 × 6 cm. All the plates were contained in sand molds with nominal dimensions of 59 × 29 × 15.5 cm, respectively.

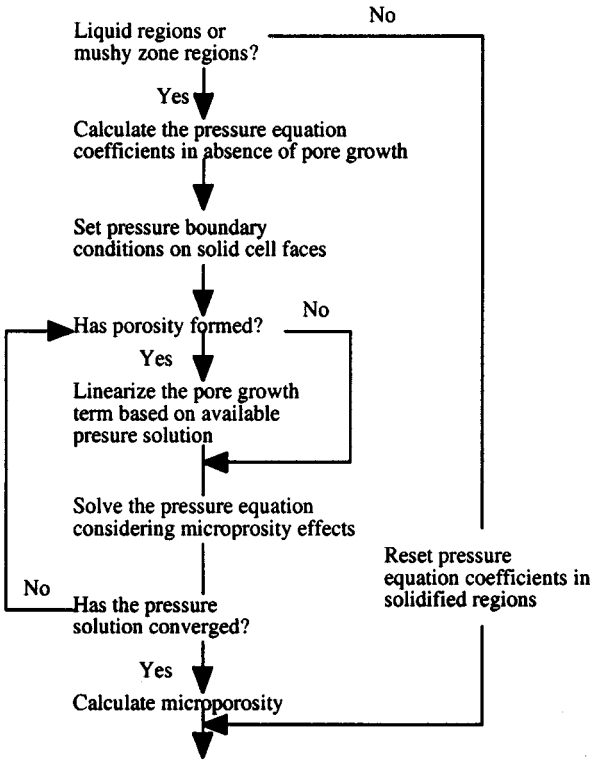

Fig. 1—Computational cycle for computing the interdendritic pressure and microporosity growth.

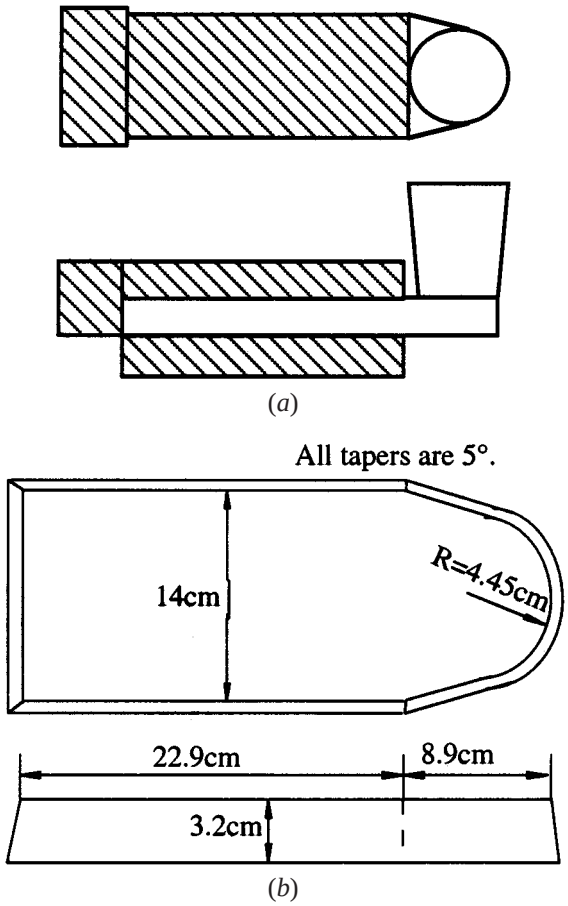

Fig. 2—Schematic illustration of (*a*) chill plate configuration and (*b*) plate dimensions.

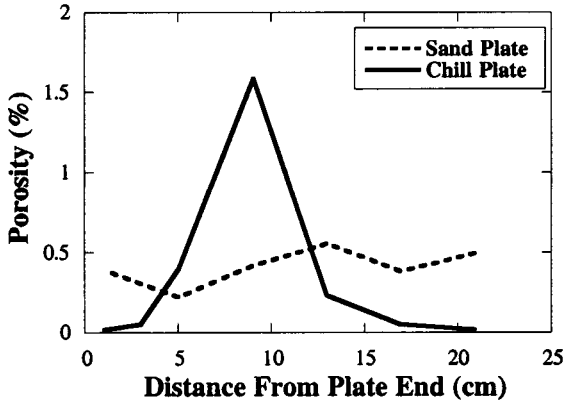

Fig. 3—Measured microporosity distribution in the sand and chill plates.

A. *Porosity Distributions in Plate Castings*

The microporosity distributions in the sand and chill plates were measured using image analysis in a separate study[37] and are shown in Figure 3. No data were reported for porosity levels in the end-chilled plate. In the aforementioned study, specimens approximately 1 cm in length were cut along the plate centerline. The porosity fraction in each sample was measured at the specimen face that corresponded to a vertical cross section thorough the plate centerline. No material was removed from the top and bottom surfaces of the specimens, and the surface-fraction porosity for each sample was computed by averaging the pore-fraction data for the individual metallographic fields over the entire surface of the sample.

As shown in Figure 3, the porosity level in the sand plate is uniform and approximately equal to 0.5 pct. The porosity levels in the chill plate are very low near the plate end and near the riser. However, the porosity exhibits a maximum of over 1.5 pct at the center of the plate. Measurements of the hydrogen concentration in the sand and chill plates indicated a level of approximately 0.112 cc/100 g (0.1 ppm) in both plates.

B. *Pore Morphology*

Figure 4 shows optical micrographs illustrating the pore morphology in three regions along the centerline of the chill plate at locations of 2.5, 11.4, and 20.3 cm from the end of the plate. All the micrographs were taken on specimen surfaces along the centerline of the chill plate. In regions close to the end of the plate and close to the riser, where the porosity level is relatively low, the pores are small and rounded and are approximately the same size as the local dendrite cell spacing (Figures 4(a) and (c)). In the middle of the plate, where the porosity level is high, the pores are large, irregular, and conform to the morphology of the interdendritic region (Figure 4(b)). In foundry terminology, the pores shown in Figures 4(a) and (c) are considered to be hydrogen porosity, while the pore morphology shown in Figure 4(b) is considered to be shrinkage porosity. The pore morphology over the entire length of the sand and end-chill plates was similar to that in Figure 4(a), corresponding to hydrogen porosity.

X. NUMERICAL SIMULATION RESULTS

Numerical simulation results are presented for aluminum A356 alloy plate castings. The mold-filling phase was

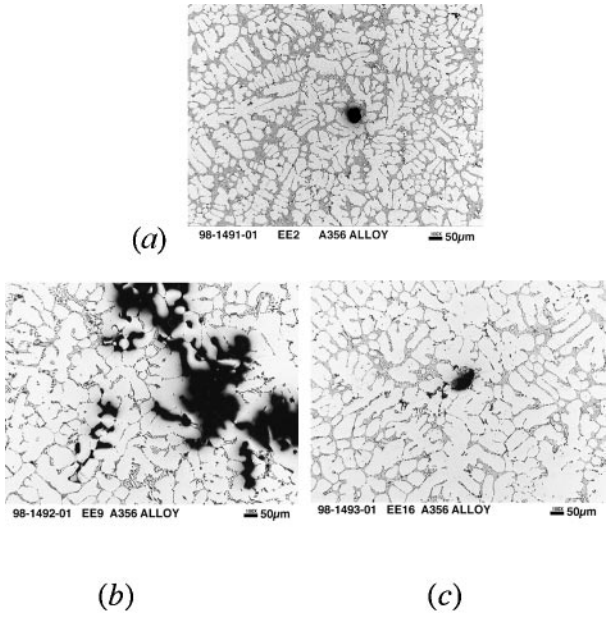

Fig. 4—Optical micrographs illustrating the pore morphology along the centerline of the chill plate at distances of (*a*) 2.5 cm, (*b*) 11.4 cm, and (*c*) 20.3 cm from the plate end.

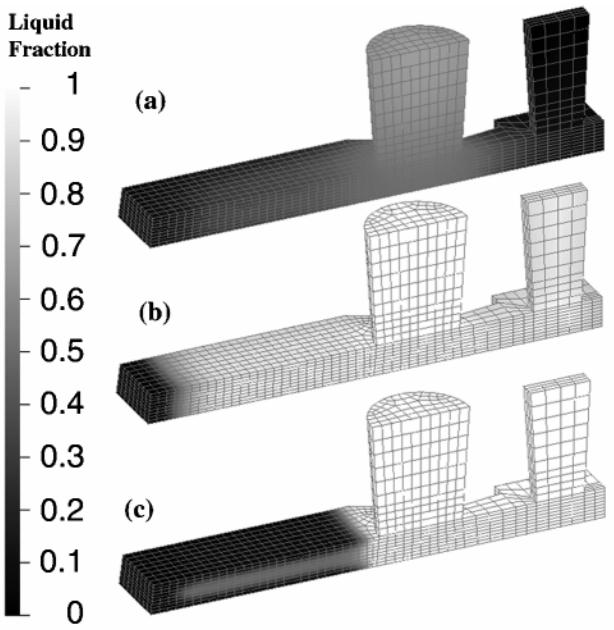

Fig. 5—Liquid fraction distributions for (*a*) sand plate at 700 s, (*b*) end-chill plate at 100 s, and (*c*) chilled plate at 30 s, since the onset of solidification.

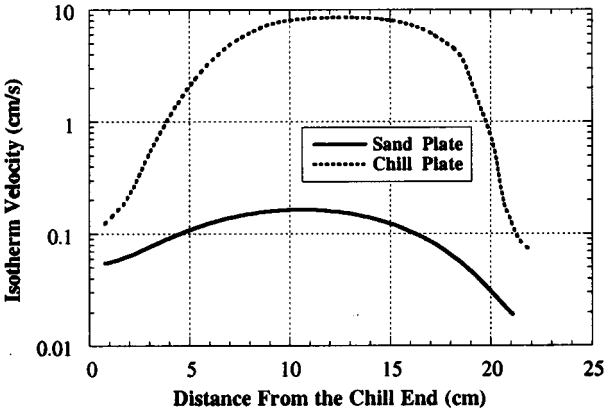

Fig. 6—Computed eutectic isotherm velocity for the sand and chill plates.

neglected in the numerical simulations, and the initial temperature of the alloy was considered to be uniform over the entire casting at 720 °C. For this study, thermophysical property data for the A356 alloy[38] were measured or estimated. The data used for estimating the density of the liquid and solid phases were measured using a dual push-rod dilatometer, the thermal conductivity was measured using a laser-flash diffusivity technique, and the specific heat and latent heat of solidification were measured by differential scanning calorimetry.[38] The solubility of hydrogen was based on data available in the literature for the aluminum-silicon system.[39] The solid volumetric fraction as a function of temperature was determined using ThermoCalc and a 12-element thermodynamic database.[38] The evolutions of the silicon and magnesium concentrations in the liquid alloy as a function of temperature were calculated using ThermoCalc and DICTRA*.[38] The surface tension was taken to be 640 dynes/cm.[40]

*DICTRA is a trademark of Thermocalc Software, Stockholm, Sweden SE-113 47.

The energy equation was solved by the use of an enthalpy formulation,[41] in which the effect of fluid convection was neglected. Due to the symmetry along the vertical cross section through the plate centerline, the problem was solved on only half of the domain.

A. *Solidification Behavior*

Due to the variation in heat extraction in the mold configurations used, the solidification behavior of the three plates considered is very different. Figure 5 shows the liquid-volume-fraction distributions for the sand plate, end-chill plate, and chill plate, at 700, 100, and 30 seconds from the onset of solidification. At these times, the end of the plate has solidified for each of the plates considered. In all plates, solidification progresses from the end of the plate toward the riser without forming any hot spots. The liquid-fraction distribution in the sand plate is the most uniform among the three plates. The solidus isotherm in the end-chill plate is planar during the entire solidification. In the chill plate, the solidification front takes the form of a channel that extends over the entire length of the plate (Figure 5(c)).

In addition, cooling rates in the sand plate are small, around 0.1 °C/s, and the eutectic isotherm velocity is quite small (Figure 6). The cooling rates in the chill plate are high, around 2 °C/s, and the resultant eutectic isotherm velocity is very large, around 10 cm/s (Figure 6). The eutectic isotherm velocity exhibits a maximum in the center of the plate, and this value is almost two orders of magnitude higher than those at the plate ends. The large isotherm velocity in the center of the chill plate indicates a sudden increase in the feeding demand in this region of the plate. Note that this corresponds to the region of high porosity in the center of the chill plate.

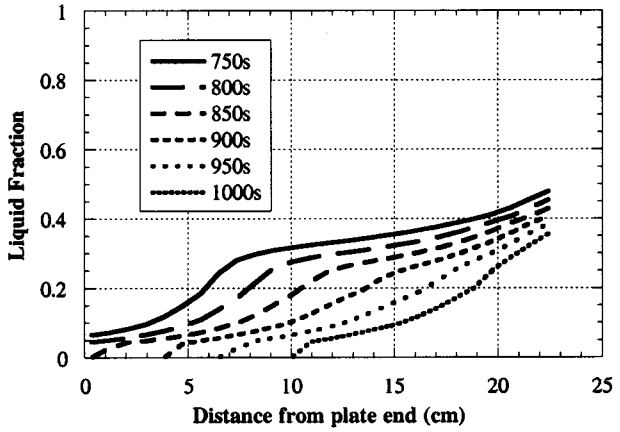

(*a*)

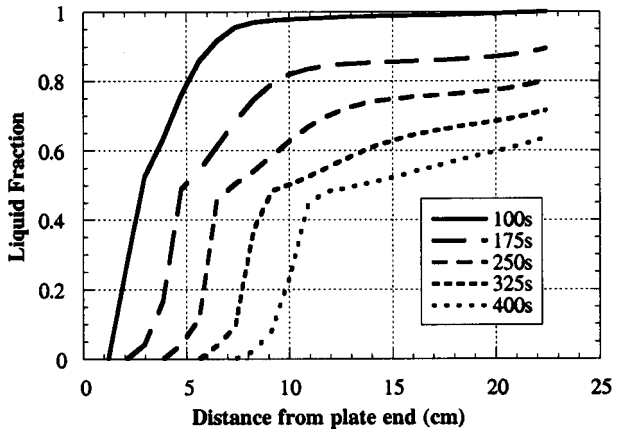

(*b*)

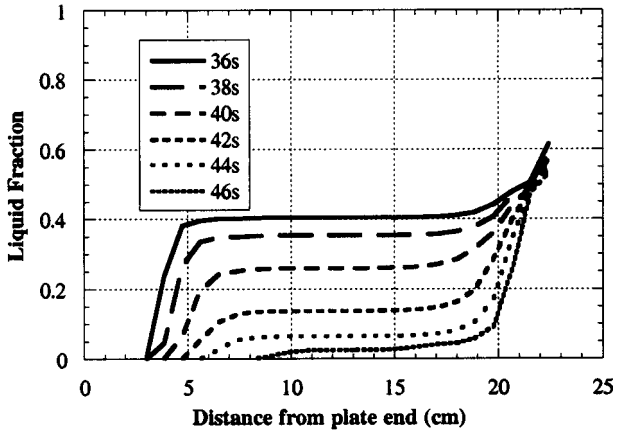

(*c*)

Fig. 7—Liquid fraction distribution along the plate centerline for the (*a*) sand plate, (*b*) end-chill plate, and (*c*) chill plate.

By analyzing the liquid-fraction profile along the plate centerline, additional confirmation of the feeding conditions in the three plates can be obtained. Figure 7 shows the evolution of the liquid-fraction profile along the plate centerline for the three plate castings considered in this study.

The liquid-fraction gradient in the sand plate is low and uniform over the length of the plate during the entire solidification. It varies from 0.05 at the end of the plate to 0.5 near the riser (Figures 5(a) and 7(a)). Although the entire casting is mushy, liquid feeding is still possible, as there is a small thermal gradient over the entire length of the plate. In the end-chilled plate, the liquid-fraction gradient at the solidification front is high, indicating good feeding conditions. Since the liquid-fraction gradient at the solidification front in the end-chill plate is higher than that in the sand plate, the feeding resistance in the end-chill plate is likely to be less than that for the sand plate. The planar-solidification isotherms and high-liquid-fraction gradient in the end-chill plate yield the best feeding conditions among the plates considered. In the chill plate, good feeding conditions are expected near the plate end and near the riser, since high-liquid-fraction gradients exist at the solidification front at these locations. In the center of the chill plate, however, the liquid-fraction gradient is almost zero and the isotherm velocity is very high, and feeding conditions are expected to be very poor. In fact, liquid-fraction gradients in the chill plate are lower than in the sand plate at the center of the plate.

The liquid-fraction contours, eutectic isotherm velocity profile, and liquid-fraction profiles all provide qualitative confirmation of the experimentally determined porosity distributions in the plate castings. The porosity level is highest in the center of the chill plate, where the worst feeding conditions are indicated, *i.e.*, a low thermal gradient and high isotherm velocity. The porosity distribution in the sand plate is fairly uniform, which is consistent with the uniform thermal conditions. The porosity levels in the end-chilled plate are expected to be the lowest among the three plates.

B. *Pressure Evolution during Solidification*

The evolution of the pressure distribution along the plate centerline as a function of time is shown in Figure 8 for the three castings considered in this study. No pressure drop is exhibited in either the sand or the end-chill plate during solidification (Figures 8(a) and (b)). However, significant pressure drops are exhibited in the chill plate (Figure 8(c)).

In Figure 9, the evolution of the local pressure as a function of liquid fraction in two computational cells is shown for the chill plate. The two cells considered are located along the centerline of the chill plate, near the plate end and plate center, at distances of 1.3 and 11 cm from the plate end. The two cells correspond to the regions shown in Figures 4(a) and (b), respectively. We note that in the cell corresponding to a region characterized by spherical pores, *i.e.*, hydrogen porosity, the pressure drop is gradual until the end of solidification. In addition, the pressure does not approach the cavitation pressure until the end of solidification. However, in the cell corresponding to a region where shrinkage porosity is observed experimentally, a severe pressure drop occurs relatively early in the solidification (*i.e.*, at a liquid fraction of 0.5), and the cavitation pressure is reached at a liquid fraction of 0.35. We can, thus, identify the regions where shrinkage porosity is observed experimentally as regions in which a severe pressure drop occurs and in which the cavitation pressure is reached relatively early during solidification.

C. *Porosity Growth during Solidification*

The appearance of hydrogen- and shrinkage-porosity regions, which are observed experimentally, can now be explained based on the evolution of the interdendritic liquid

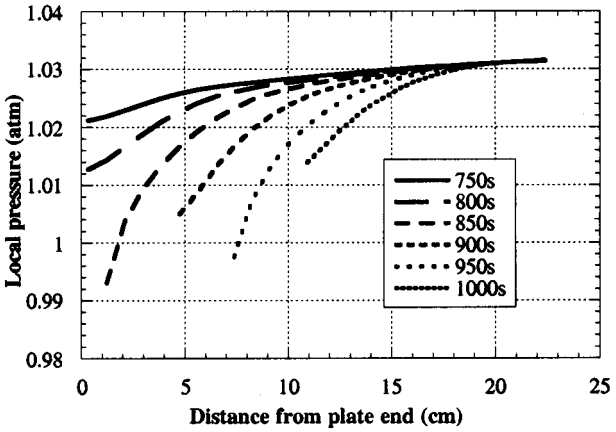

(*a*)

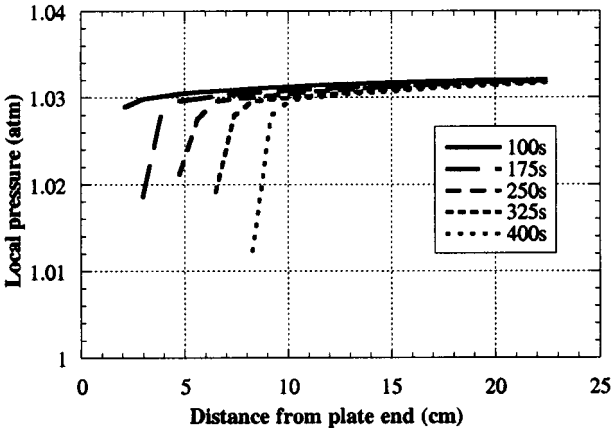

(*b*)

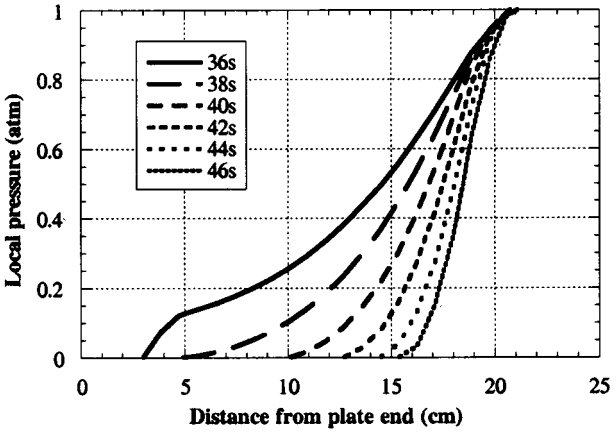

(*c*)

Fig. 8—Pressure distribution along the plate centerline for the (*a*) sand plate, (*b*) end-chill plate, and (*c*) chill plate.

pressure during solidification. As the partial pressure of hydrogen, which corresponds to the hydrogen concentration within the liquid, overcomes the local liquid pressure and surface-energy forces, the hydrogen porosity nucleates. Immediately following their nucleation, hydrogen pores expand into bubbles of regular shape that occupy a region between dendrite cells (or between grains). If this occurs toward the end of solidification, there is little further pore growth, and the final pore size upon solidification is proportional to the local dendrite cell spacing. These are the pores

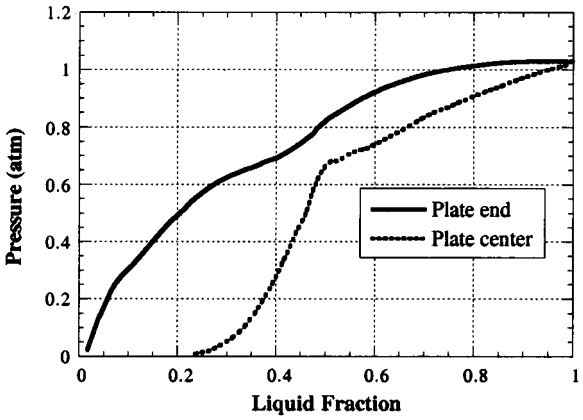

Fig. 9—Pressure evolution during solidification at locations near the plate end and plate center.

that are typically characterized as hydrogen porosity. In fact, this inevitably occurs during the solidification of aluminum alloys, since some hydrogen is always present in solution and segregates to the last liquid to freeze, and it is eventually enriched beyond the solubility limit.

In regions of inadequate feeding, a severe pressure drop occurs early in solidification, yielding hydrogen bubble nucleation early in solidification. As solidification proceeds, there is further demand for feed metal. If the resistance to liquid flow is high, the amount of liquid feeding is insufficient to compensate for the entire shrinkage, and the spherical hydrogen pores expand into the irregular interdendritic region to compensate for solidification shrinkage. This also accounts for the interdendritic morphology of shrinkage porosity. Under these conditions, although hydrogen bubble nucleation occurs as hydrogen is present in solution and the condition for microporosity formation is reached (Eq. [11]), the actual pressure drop may reach the cavitation pressure for the liquid (Figure 9). Consequently, pore nucleation could occur even if hydrogen is not present.

The previous analysis suggests that the categorization of pores as being due to hydrogen or shrinkage effects is actually quite accurate. In the chill plate, both types of porosity are present, as the plate contains regions of both good and poor feeding. In the sand plate, the pore morphology at all locations along the plate corresponds to that of hydrogen porosity, as solidification is uniform and progressive (*i.e.*, there are no hot spots) and no region of excessive metal demand is encountered. The pore morphology in the end-chill plate also corresponds to that of hydrogen porosity, as the feeding conditions in the end-chill plate are good.

D. *Shrinkage-Porosity Computation during Solidification*

By considering that interdendritic feeding takes place until the end of solidification and that the pore fraction is given by the hydrogen mass balance and Sievert's law (*i.e.*, Eq. [12]), the *computed* liquid pressure in poorly fed regions can drop below zero absolute pressure. This occurs because the interdendritic liquid cannot feed the entire solidification shrinkage in regions of severe shrinkage. If the liquid continues to feed the solidification shrinkage in those regions, the pressure drops to values lower than the cavitation pressure.

Therefore, once the liquid pressure in a computational cell reaches the cavitation pressure, the pressure in that cell is set to the cavitation pressure until the end of solidification, assuming that liquid feeding is negligible. In general, the cavitation pressures of liquid metals at casting temperatures are very small. At casting temperatures of around 750 °C, the cavitation pressure for pure aluminum was determined from published data[42] to be approximately 10^{-6} atm.

For the computation of microporosity in this study, the porosity growth before the pressure reaches the cavitation point is considered to be that of hydrogen porosity. The interdendritic liquid pressure during solidification decreases with the liquid fraction until the cavitation point is reached. At pressures greater than the cavitation pressure, the pore-fraction evolution is described by the hydrogen mass conservation and Sievert's law (Eq. [12]). After the liquid reaches the cavitation pressure, the use of Eq. [12] to describe the pore evolution is inappropriate. If Sievert's law was used to calculate the pore fraction, the gas pressure would be given by $P_g = P_c + P_\sigma$, and the porosity would grow only as P_σ drops due to coarsening effects (Eq. [10]). This amount of pore growth, which would be solely due to the effect of dendrite coarsening on P_σ, would not compensate for the entire solidification shrinkage, and the mass conservation would be violated.

Consequently, in severe shrinkage regions in the mushy zone, *i.e.*, where the liquid pressure has reached the cavitation pressure, porosity is determined such that it compensates for the entire solidification shrinkage within the current time step:

$$g_g^{n+1} = g_g^n + \frac{\overline{\rho}^{*n+1} - \overline{\rho}^n}{\overline{\rho}^{*n+1}} (1 - g_g^n) \qquad [36]$$

Because no feeding is considered to take place in computational cells in which the pressure has reached the cavitation pressure, the pressure is not computed in these cells. Also, the pressure boundary-condition equation (Eq. [8]) is now imposed at the interfaces between the mushy zone and cavitated regions. Accordingly, the computational cycle is changed, as shown in Figure 10.

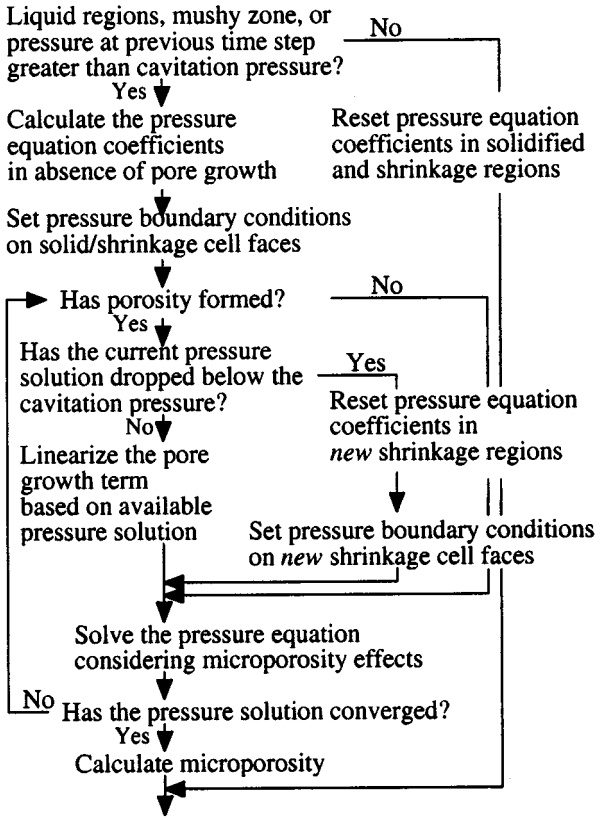

Fig. 10—Computational cycle that includes hydrogen porosity and severe shrinkage regions.

E. *Porosity Distributions in Plate Castings*

The computed microporosity distribution at the end of solidification is shown in Figure 11 for the three castings considered. The results presented are for a hydrogen content of 0.112 cc/100 g. The microporosity distributions are shown for one-quarter of the plate, and both horizontal and vertical cross sections through the plate centerline are visible. The riser is on the right-hand side of the plate, at a distance approximately 21 cm from the plate end.

The computed results for the porosity distribution along the plate centerline are also plotted in Figure 12, along with the experimentally measured values. The value at each computed point corresponding to the experimental measurement was obtained by averaging the *volumetric* porosity fractions over the computational cells representing the sample area. This was necessary, as the numerical simulation only yields a single value of porosity fraction for each computational cell.

However, this is not expected to introduce a significant error, since porosity does not vary significantly in the direction normal to the vertical symmetry plane of the plate (Figure 11).

Both Figures 11 and 12 show that the porosity level in the sand plate is fairly uniform and is around 0.5 pct. The porosity level in the end-chill plate increases gradually from 0.4 pct at the chill end to 0.5 pct near the riser (Figure 11). The porosity distribution for the chill plate exhibits a peak in the center of the plate.

The numerical results qualitatively reproduce the microporosity profiles obtained from image-analysis measurements. For the sand plate, there is good agreement between the measured and computed porosity. The porosity level in the sand plate is seen to be fairly uniform over the entire plate in both the experimental and computed results. The porosity level in the chill plate exhibits a maximum at the center of the plate. The prediction of a high-porosity region in the center of the chill plate is in good agreement with experimental results. The location of the peak in the porosity distribution is also consistent with the solidification behavior (Figures 5 through 7) and the ensuing evolution of the interdendritic feeding (Figures 8 and 9).

In addition to the microporosity profile, there is good agreement between the numerical simulation results and experimental results on the presence and location of hydrogen and shrinkage porosity. In agreement with experimental observations, the numerical simulation predicts hydrogen porosity over the entire sand plate, since there is no significant pressure drop in the plate (Figure 8(a)) and no shrinkage-porosity growth. In the chill plate, both hydrogen and shrinkage porosity are present, as the plate contains

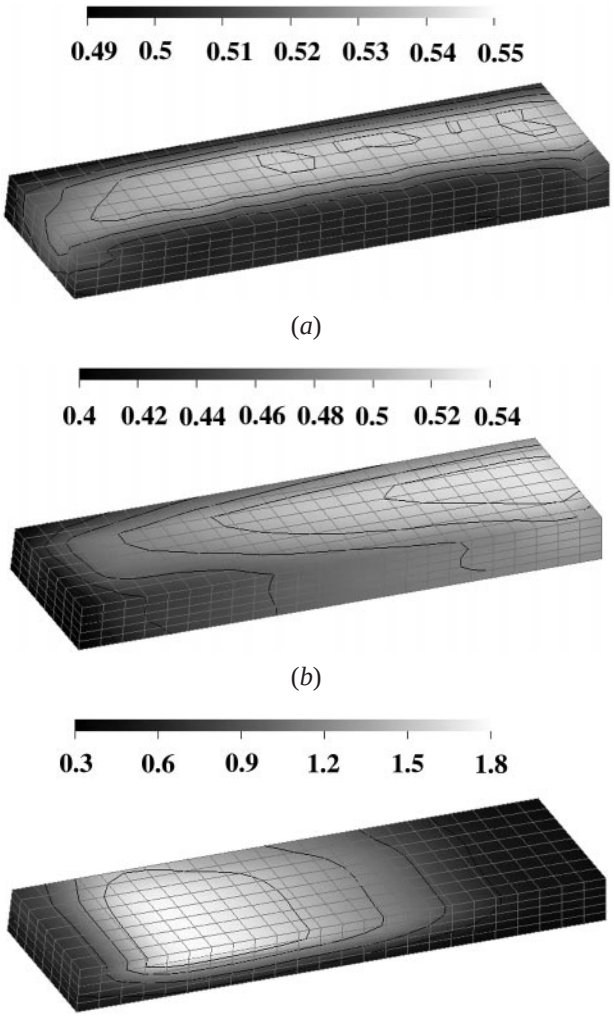

Fig. 11—Porosity distribution in the lower quarter of the (*a*) sand plate, (*b*) end-chilled plate, and (*c*) chilled plate.

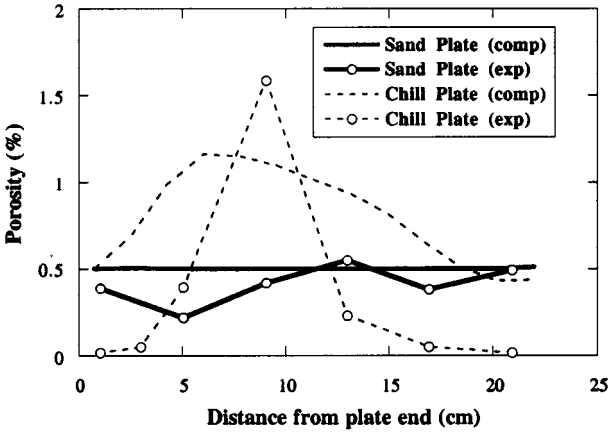

Fig. 12—Measured and computed microporosity distributions along the plate centerline.

regions of both good and poor feeding (Figure 9). This suggests that the assumptions in the model regarding the conditions for formation of hydrogen and shrinkage porosity are valid.

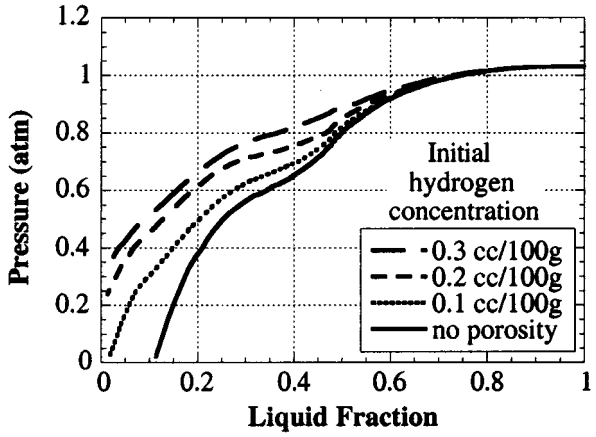

Fig. 13—Pressure evolution during solidification at a location near the plate end for different initial hydrogen concentrations.

Some differences between the experimental measurements and the numerical simulation must also be noted. In the case of the chill plate, the model correctly predicts the maximum in porosity near the center of the plate. However, the predicted minimum porosity is higher, the predicted maximum porosity is lower, and the peak in the distribution is broader than in the experimental results. These differences can be attributed to several factors. One factor is the accuracy of properties that have an important effect on microporosity, such as alloy density and hydrogen solubility. Alloy density is critical, since the density variation during solidification drives the shrinkage demand. Although significant effort was expended in this study to quantify the density variation, no experimental data were available to estimate the liquid- and solid-phase densities in the last stages of solidification, *i.e.*, during the formation of the ternary eutectic. It was determined from a thermodynamic analysis that magnesium was strongly segregated to the liquid in the final stages of solidification. It might be expected that magnesium would have a strong effect on the density, and data in the literature[43] suggest that magnesium also has a strong effect on hydrogen solubility. Another important factor that affects microporosity is the pore curvature. In this study, the radius of the pore is assumed to be proportional to the average dendrite cell spacing for a particular location. However, in reality, the pore curvature will be determined by the local microstructure, and adjacent pores may well have different radii. Finally, two phenomena that affect the final porosity are neglected in this model. One is hydrogen diffusion, and the other is pore migration. Recent studies[32] suggest that hydrogen diffusion likely plays an important role in pore formation. Also, a study on transparent materials indicated that pore migration becomes important at the high thermal gradients expected in the chill plate.[32]

F. *Effect of Porosity on the Fluid Flow*

In order to illustrate the effect of porosity on the fluid flow, the evolution of pressure during solidification is shown for different initial hydrogen concentrations. The pressure evolution is analyzed for the two computational cells in the chill plate considered previously in Section X–B. The results also include the case in which porosity formation is not considered.

Figures 13 and 14 show the evolution of the local pressure

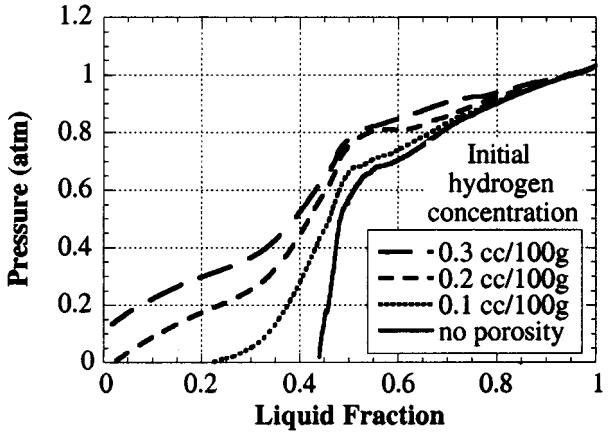

Fig. 14—Pressure evolution during solidification at a location near the plate center for different initial hydrogen concentrations.

in each cell as a function of liquid fraction for different initial hydrogen concentrations. Without considering porosity formation, the pressure reaches the cavitation pressure at about 10 and 35 pct liquid, respectively. When porosity formation is considered, higher pressures are obtained. The higher pressures obtained when microporosity is considered are due to the fact that microporosity partially compensates for the solidification shrinkage, reducing the feeding demand. A reduced feeding demand results in lower pressure drops, *i.e.*, higher pressures in the mushy zone.

As the amount of hydrogen is increased, the onset of shrinkage-porosity growth occurs at larger solid fractions. At very high hydrogen concentrations, *i.e.*, 0.3 cc/100 g, the pressure does not reach the cavitation pressure and only hydrogen-porosity formation is predicted, without shrinkage porosity. The fact that that at very high hydrogen contents the porosity becomes evenly distributed is supported by foundry experience.

The analysis of the pressure evolution during solidification shows that the effect of microporosity on the fluid flow cannot be neglected. If the effect of microporosity on the fluid flow is neglected, the pressure is underpredicted and microporosity is overpredicted.

XI. CONCLUSIONS

A comprehensive methodology for the prediction of the microporosity fraction is presented. The solution algorithm presented includes a fully coupled, implicit treatment of local pressure and microporosity evolution in the mushy zone. The methodology presented takes into account solidification, shrinkage-driven interdendritic fluid flow, hydrogen precipitation, and porosity evolution during solidification. Porosity formation and its growth due to both hydrogen precipitation and solidification shrinkage are considered. Microporosity formation and growth are due to the local pressure drop in the mushy zone, and shrinkage porosity is assumed to occur by pore expansion in regions where solidification shrinkage cannot be compensated for by the interdendritic fluid flow. The analysis of the pressure evolution during solidification shows that the effect of microporosity on the fluid flow cannot be neglected. It is also shown that the calculation of the local pressure during solidification can be used to identify and predict the conditions for the formation of hydrogen and shrinkage porosity. The solution algorithm presented has been implemented in a computational framework consistent with those of commercial casting codes.

The methodology presented has been validated on test castings designed to capture a variety of solidification conditions and porosity distributions. The numerical results reproduce the characteristic microporosity profiles observed in the experimental results and also agree quantitatively with the experimentally measured porosity levels. However, the predicted minimum porosity is higher, the maximum predicted porosity is lower, and the peak in the porosity distribution is broader than those shown in the experimental results. In addition, the prediction of regions of hydrogen and shrinkage porosity is in good agreement with experimental results. Numerical simulation results also indicate that at very high hydrogen contents, shrinkage porosity can be suppressed so that only evenly distributed hydrogen porosity is obtained.

The differences between the experimental measurements and computed results are attributed to uncertainties in the density values used for the liquid, especially in the region of the final ternary eutectic; the difference in the solubility of hydrogen in complex alloys compared to that in binary alloys; the assumptions in pore radius; and the effects of pore migration during solidification. The quantitative prediction of porosity levels in production castings provides an enhanced capability for the design of structural safety critical components.

ACKNOWLEDGMENTS

This work was performed under a Cooperative Research and Development Agreement (CRADA) with the United States Advanced Materials Partnership (USAMP), United States Council for Automotive Research (USCAR) for the project on Design and Product Optimization for Cast Light Metals. This research was sponsored by the United States Department of Energy, Assistant Secretary for Energy Efficiency and Renewable Energy, Office of Transportation Technologies, Lightweight Vehicle Materials Program and Office of Heavy Vehicle Technologies, under Contract No. DE-AC05-96OR22464 with Lockheed Martin Energy Research Corp. and DE-AC05-00OR22725 with UT–Battelle, LLC. This research was supported, in part, by appointments to the Oak Ridge National Laboratory Postdoctoral Research Associates Program, administered jointly by the Oak Ridge Institute for Science and Education and Oak Ridge National Laboratory. The authors also thank D.B. Kothe (Los Alamos National Laboratory), for providing access to the Telluride code for the computations done in this study; Q. Han and S.R. Agnew for reviewing the paper; and M.L. Atchley for preparing the manuscript.

REFERENCES

1. T.S. Piwonka and M.C. Flemings: *Trans. AIME*, 1966, vol. 236, pp. 1157-65.
2. H.F. Bishop and W.S. Pellini: *Trans. AFS*, 1950, vol. 58, pp. 185-87.
3. E. Niyama, T. Uchida, M. Morikawa, and S. Saito: *AFS Int. Cast Met. J.*, 1981, vol. 6, pp. 16-22.
4. Y.W. Lee, E. Chang, and C.F. Chieu: *Metall. Trans. B*, 1990, vol. 21B, pp. 715-22.

5. V.K. Suri, H. Huang, J.T. Berry, and J.L. Hill: *Trans. AFS*, 1992, vol. 100, pp. 399-407.
6. S. Viswanathan, V.K. Sikka, and H.D. Brody: *JOM*, 1992, Sept., pp. 37-40.
7. S. Viswanathan and H.D. Brody: *Trans. AFS*, 1992, vol. 100, pp. 685-96.
8. W.D. Walther, C.M. Adams, and H.F. Taylor: *Trans. AFS*, 1956, vol. 64, pp. 658-64.
9. K. Kubo and R.D. Pehlke: *Metall. Trans. B*, 1985, vol. 16B, pp. 359-66.
10. D.R. Poirier, K. Yeum, and A.L. Maples: *Metall. Trans. A*, 1987, vol. 18A, pp. 1979-87.
11. M. Barkhudarov, H. Hou, J. Ortega, J. Beech, S.B. Chin, and D.H. Kirkwood: *Modeling of Casting, Welding, and Advanced Solidification Processes—VI*, T.S. Piwonka, V. Voller, and L. Katgerman, eds., TMS, Warrendale, PA, 1993, pp. 421-34.
12. V.K. Suri and A.J. Paul: *Trans. AFS*, 1993, vol. 101, pp. 949-54.
13. Q.T. Fang and D.A. Granger: *Trans. AFS*, 1989, vol. 97, pp. 989-1000.
14. S. Shivkumar, D. Apelian, and J. Zou: *Trans. AFS*, 1990, vol. 98, pp. 897-904.
15. G.K. Sigworth and C. Wang: *Metall. Trans. B*, 1993, vol. 24B, pp. 365-77.
16. J. Huang, T. Mori, and J.G. Conley: *Metall. Mater. Trans. B*, 1998, vol. 29B, pp. 1249-60.
17. H. Combeau, D. Carpentier, J. Lacaze, and G. Lesoult: *Mater. Sci. Eng.*, 1993, vol. A173, pp. 155-59.
18. P. Rousset, M. Rappaz, and B. Hannart: *Metall. Mater. Trans A*, 1995, vol. 26A, pp. 2349-58.
19. J. Zou and R. Doherty: *Modeling of Casting, Welding, and Advanced Solidification Processes—VI*, T.S. Piwonka, V. Voller, and L. Katgerman, eds., TMS, Warrendale, PA, 1993, pp. 193-200.
20. H. Combeau, A. Bourg, J. Charbonnier, S. Langlois, G. Lesoult, C. Rigaut, and C. Sztur: *Modeling of Casting, Welding, and Advanced Solidification Processes VII*, M. Cross and J. Campbell, eds., TMS, Warrendale, PA, 1995, pp. 67-75.
21. A.V. Kuznetsov and K. Vafai: *Int. J. Heat Mass Transfer*, 1995, vol. 38, pp. 2557-67.
22. S. Sundarraj and V.R. Voller: *Int. J. Heat Mass Transfer*, 1995, vol. 38, pp. 1009-18.
23. L. Arnberg, L. Backerud, and G. Chai: *Solidification Characteristics of Aluminum Alloys, Vol. 3: Dendrite Coherency*, AFS, Des Plaines, IL, 1996, p. 8.
24. J. Campbell: *Castings*, Butterworth-Heinemann, Oxford, United Kingdom, 1991, p. 192.
25. S. Chang and D.M. Stefanescu: *Acta Mater.*, 1996, vol. 44, pp. 2227-35.
26. A.V. Reddy and C. Beckermann: *Metall. Mater. Trans. B*, 1997, vol. 28B, pp. 479-89.
27. C. Beckermann and R. Viskanta: *Appl. Mech. Rev.*, 1993, vol. 46, pp. 1-27.
28. K. Murakami and T. Okomoto: *Acta Metall.*, 1984, vol. 32, pp. 1741-44.
29. D.R. Poirier and S. Ganesan: *Mat. Sci. Eng. A*, 1992, vol. A157, pp. 113-23.
30. P. Ocansey, M.S. Bhat, D.R. Poirier, and T.L. Finn: *Light Metals*, U. Mannweiler, ed., TMS, Warrendale, PA, 1994, pp. 807-12.
31. A. Duncan, Q. Han, and S. Viswanathan: *Metall. Mater. Trans. B*, 1999, vol. 30B, pp. 745-50.
32. Q. Han and S. Viswanathan: Oak Ridge National Laboratory, Oak Ridge, TN, unpublished research, 1999.
33. A.S. Sabau, Q. Han, and S. Viswanathan: in *Fluid Flow Phenomena in Metals Processing*, N. El-Kaddah, D.G.C. Robertson, S.T. Johansen, and V.R. Voller, eds., TMS, Warrendale, PA, 1999, pp. 403-11.
34. Y.W. Lee, E. Chang, and C.F. Chieu: *Mater. Sci. Eng. A*, 1990, vol. A124, pp. 233-40.
35. I.J. Chiou and H.L. Tsai: *Trans. AFS*, 1990, vol. 98, pp. 823-30.
36. M.C. Flemings: *Solidification Processing*, McGraw-Hill, New York, NY, 1974, p. 150.
37. M.D. Dighe, X.G. Jiang, A. Tewari, A.S.B., Rahardjo, and A.M. Gokhale: *Trans. AFS*, 1998, vol. 106, pp. 181-90.
38. S. Viswanathan, A.S. Sabau, W.D. Porter, R.B. Dinwiddie, and Q. Han: Oak Ridge National Laboratory, Oak Ridge, TN, unpublished research, 1999.
39. W.R. Opie and N.J. Grant: *Trans. AIME, J. Met.*, 1950, vol. 188, pp. 1237-41.
40. D. Emadi, J.E. Gruzleski, and J.M. Toguri: *Metall. Trans. B*, 1993, vol. 24B, pp. 1055-63.
41. A.V. Reddy, D.B. Kothe, C. Beckermann, R.C. Ferrell, and K.L. Lam: *Proc. 4th Decennial Int. Conf. on Solidification Processing*, J. Beech and H. Jones, eds., The University of Sheffield, Sheffield, United Kingdom, 1997, pp. 83-87.
42. *CRC Handbook of Chemistry and Physics*, 70th ed., R.C. Weast, ed., CRC Press, Boca Raton, FL, 1989, p. D-217.
43. P.N. Anyalebechi: *Scripta Metall. Mater.*, 1995, vol. 33, pp. 1209-16.